Journal of Photonics for Energy

PhotonicsforEnergy.SPIEDigitalLibrary.org

Incorporation of nanocrystals with different dimensionalities in hybrid TiO_2/P3HT solar cells

Flavio Santos Freitas
Juliana Martins de Souza e Silva
Mateus Borba Cardoso
Ana Flavia Nogueira

SPIE.

Incorporation of nanocrystals with different dimensionalities in hybrid TiO_2/P3HT solar cells

Flavio Santos Freitas,[a] Juliana Martins de Souza e Silva,[b] Mateus Borba Cardoso,[b] and Ana Flavia Nogueira[a,*]

[a]University of Campinas–UNICAMP, Institute of Chemistry, Laboratory of Nanotechnology, and Solar Energy, P.O. Box 6154, Campinas SP 13083-970, Brazil

[b]Brazilian Center for Research in Energy and Materials–CNPEM, Brazilian Synchrotron Light Laboratory–LNLS, Campinas SP 13083-970, Brazil

Abstract. We investigate the effect of TiO_2 nanoparticles–nanospheres and nanorods–inserted in the poly(3-hexylthiophene) (P3HT) matrix of TiO_2/P3HT inverted hybrid solar cells. X-ray diffraction, high-resolution transmission electron microscopy, small-angle x-ray scattering, photoluminescence, and photoelectrochemical experiments were employed to investigate the structure, morphology, and photoactivity of TiO_2 nanoparticles modified with 2-thiopheneacetic acid, mixed or not with P3HT. Both TiO_2 nanospheres and TiO_2 nanorods presented a good dispersion in the polymer matrix. The incorporation of TiO_2 nanospheres and nanorods has improved the photocurrent generation, and devices with efficiency values up to 1.35% were obtained. Our results reveal that the nanoscale morphology enables an enhanced interfacial area for exciton dissociation. In particular, the nanospheres contribute with their high specific area, and the nanorods contribute with their high aspect ratio. © *2015 Society of Photo-Optical Instrumentation Engineers (SPIE)* [DOI: 10.1117/1.JPE.5.057407]

Keywords: hybrid solar cell; TiO_2 nanospheres; TiO_2 nanorods; poly(3-hexylthiophene) (P3HT).

Paper 14091SS received Nov. 2, 2014; accepted for publication Feb. 6, 2015; published online Feb. 25, 2015.

1 Introduction

Polymer/inorganic nanocrystal hybrid solar cells have drawn considerable attention as a promising photovoltaic technology for the future. These hybrid solar cells have several advantages over their pure inorganic counterparts: lower production costs through solution processing, greater mechanical flexibility, lighter weight, and additional versatility provided by the ability to control the shape and size of the inorganic nanocrystals.[1,2] Specifically, metal oxides have outstanding chemical and physical stabilities, high electron mobility, high dielectric constant, and low-cost, and most of them are environmentally friendly.[3,4]

The combination of TiO_2 and poly(3-hexylthiophene) (P3HT) as electron-acceptor and electron-donor materials, respectively, is an example of a good candidate of hybrid solar cells. TiO_2 spherical nanocrystals are very interesting and intensely exploited as mesoporous electrodes in dye sensitized solar cells. One-dimensional (1-D) TiO_2 nanorods with high aspect ratios have additional advantages as these structures provide a direct pathway for electron transport and can be synthesized by simple sol-gel method at low temperature.[5,6]

The strong coupling between the positive and negative charges found in the polymer excitons requires these excitons to diffuse to an interface in order to dissociate into free charges. To improve charge generation and charge transport, a mixture of TiO_2 nanoparticles in the P3HT polymer matrix were proposed to facilitate the *in situ* exciton dissociation.[7,8] In addition, inorganic nanocrystals, if well dispersed, can promote efficient charge-carrier hopping, and improvements in the electron and hole mobilities were reported.[9,10,11]

*Address all correspondence to: Ana Flavia Nogueira, E-mail: anaflavia@iqm.unicamp.br

An important feature in the polymer/nanocrystal hybrid solar cells is the presence of an interface. The incompatibility found at the organic/inorganic interfaces has been tackled by inserting interfacial (organic) modifiers in the inorganic material, which decreases the charge recombination in the device due to a more intimate contact between nanoparticles and the P3HT.[12,13] Another interesting strategy in polymer/inorganic nanocrystal hybrid solar cells is to take advantage of the wide variety in device architecture to leverage the efficiency. The bulk heterojunction concept in the normal configuration (metal/polymer+nanocrystals/PEDOT-PSS/ITO) is the preferentially adopted configuration and it also delivers the best results.[14,15] However, the lack of stability found in the normal configuration reinforces the importance of the inverted configuration where electrons and holes are collected from transparent electrodes and metal electrodes, respectively.[16] The inverted configuration exhibits significant device stability and more compatible gradient profiles that facilitate electron and hole transports.[17] Planells et al. applied this concept in hybrid solar cells (TiO_2/*(E)-2-Cyano-3-(3′,3″,3‴,3⁗-tetrahexyl-[2,2′:5′,2″:5″,2‴:5‴,2⁗-quinquethiophen]-5-yl)acrylic acid* P3HT with bis(trifluoromethanesulfonyl)imide/Ag) achieving an efficiency greater than 2%.[12] In this work, the authors also doped the P3HT polymer with bis(trifluoromethanesulfonyl)imide, which was crucial to negatively shift the TiO_2 conduction band and to improve the device's performance.[18]

Herein, we present the synthesis and characterization of TiO_2 nanoparticles in two different shapes: nanorods and spherical nanoparticles. Both nanoparticles were functionalized with thiopheneacetic acid (TAA) in order to improve the compatibility between the inorganic nanocrystals and P3HT.[13] A mixture of TiO_2 nanoparticles (spherical and nanorods) and P3HT was used as an active layer in hybrid solar cells in the inverted configuration, and the results were compared.

2 Experimental Section

TiO_2 nanorods (TiO_2 NR) were synthetized following the methodology developed by Cozzoli et al.[5] This procedure was chosen to produce well-crystallized anatase titania nanostructures of controlled size and shape, which were then dispersed in organic media with the use of oleic acid (OLEA) as a surfactant. In a three-neck flask, 60.0 g of oleic acid (Aldrich) was heated under stirring at 100°C under N_2 flux. Titanium isopropoxide (Across) was added, and the system was maintained under stirring for 5 min. The solution turned from colorless to pale yellow, indicating the formation of a complex. Then, 8.5 mL of a 17-mmol aqueous solution of trimethylamine *N*-oxide (Aldrich) was rapidly injected. The reaction was stirred under mild reflux with water for 10 to 12 h to promote further hydrolysis and crystallization of the product. The procedure for TiO_2 nanospheres preparation (TiO_2 NS) was similar; however, a slow hydrolysis was performed prior to the dissolution of trimethylamine *N*-oxide in anhydrous (50 mmol) ethylene glycol (EG). The hydrolysis of the titanium precursor was believed to occur upon reaction with water which was slowly released upon esterification of OLEA and EG. The total reaction time was 72 h due to the esterification rate likely being the bottleneck of the overall reaction rate.

At the end of both procedures, the nanoparticles were washed, precipitated, and centrifuged 10 times with methanol to remove the majority of the oleic acid. The surface modification of TiO_2 NR and NS was carried out by transferring the titania powder to a solution of 0.1 mol L^{-1} of 2-TAA and maintaining the system under reflux for 48 h (TiO_2 NR/TAA and TiO_2 NS/TAA). The nanocomposite active layer was prepared using a concentration of 15 mg mL^{-1} in chlorobenzene (Aldrich) with a 1:1 proportion between P3HT and TiO_2 NR/TAA or TiO_2 NS/TAA.

The powder x-ray diffraction (XRD) patterns were used to unveil the phase information and the crystalline quality of the prepared materials. They were collected on a Shimadzu model XRD-7000 diffractometer using Cu Kα radiation (0.154 nm) at 40 kV and 30 mA, with a rate of 2.0 min^{-1} for 2θ measurements over the range of 5 deg to 80 deg.

Raman spectra were recorded by using a Raman confocal spectrometer, T64000 model—Jobin Yvon—, with an exposure time of 30 s, accumulation of 10 spectra and 633 nm laser excitation in the 100 to 700 cm^{-1} frequency range. The absorption spectra were obtained on a diode array spectrophotometer Hewlett Packard 8452A.

The high-resolution transmission electron microscopy (HRTEM) images were obtained using a HRTEM-JEM 3010 URP microscope at an accelerating voltage of 300 kV at the electron microscopy laboratory (LME) located at the Brazilian National Nanotechnology Laboratory (CNPEM). The sample for the transmission electron microscopy (TEM) analysis was prepared by dispersing the material powder in isopropanol via sonication for 15 min, followed by drop casting onto a carbon-coated copper TEM grid (400 mesh).

Small-angle x-ray scattering (SAXS) experiments were performed at the D1B-SAXS1 beamline at the Brazilian Synchrotron Light Laboratory (LNLS) located at CNPEM. The samples were mounted as wafers between Kapton tapes. The monochromatic beam was collimated by slits with a fixed energy of 8.0 keV and a wavelength of 0.155 nm. Silver behenate was used to calibrate the sample-detector distance, equal to 1472 mm during the experiment. Transmission and dark current corrections were performed, and the isotropic scattering pattern was radially averaged. The resulting scattering patterns $I(q)$ versus q were plotted, and SAXS data analysis was carried out using Igor Pro Software (WaveMetrics) and multilevel unified fit analysis.[19,20,21]

The photoelectrochemical experiments were carried out in an Eco Chimie-Autolab PGSTAT 12 potentiostat. Chronoamperometric measurements were performed using a three-electrode configuration cell (Ag/AgCl as reference electrode, FTO/TiO_2 films as working electrodes, and a platinum wire as counter electrode), at room temperature. A 1-mol L^{-1} solution of aqueous KCl containing 5×10^{-2} mol L^{-1} methylviologen was used as the electrolyte. The photoelectrochemical cell was placed in an optical bench consisting of an Oriel Xe(Hg) 250 W lamp coupled to an AM 1.5 filter (Oriel), collimating lenses, and a water filter (Oriel). The light intensity was calibrated with an optical power meter (model 1830-C, Newport) to 100 mW cm^{-2}.

The hybrid solar cells in the inverted configuration were assembled as follows: fluorine-doped tin oxide (FTO) coated glass substrates were first cleaned in an ultrasonic bath for 10 min, using water-detergent, ethanol, and 2-propanol as solvents. For the devices, the extremities of the FTO substrates were chemically etched. A TiO_2 compact layer (50 to 80 nm) was deposited by spin coating a solution of titanium(IV) isopropoxide, ethanol, and acetylacetone at 5000 rpm for 1 min, followed by drying in air for 5 min. These films were then heated at 450°C for 20 min. A second layer of mesoporous TiO_2 consisting of the commercial TiO_2 suspension (Ti Nanoxide T, Solaronix) in ethanol (1 : 1) was spread onto the film by spin coating, and the film was heated at 450°C for 40 min (500 nm). The electrodes were immersed in a 1.5×10 mol L^{-1} solution of N719 dye (Solaronix) overnight. The nanocomposite films (thickness of ~170 to 200 nm) were deposited onto the sensitized mesoporous titania film by spin coating a suspension of P3HT and TiO_2 nanoparticles in chlorobenzene (15 mg mL^{-1} in 1 : 1 proportion). Then, the electrode film was annealed at 120°C under N_2 atmosphere following which a PEDOT:PSS layer was deposited by spin coating (~30 nm) followed by further annealing at 120°C. Finally, the system was transferred to an N_2-filled glove box, and gold top electrodes were thermally deposited through a shadow mask (thickness of ~100 nm) in high vacuum (pressure of 10^{-6} mbar).

Current versus voltage (I-V) curves were obtained through a Sciencetech solar simulator with a Xe lamp and AM 1.5 filter to generate a simulated solar spectrum (0.1 cm^2 active area in the devices). The irradiation intensity was set to 100 mW cm^{-2} and calibrated using a standard silicon PV device.

3 Results and Discussion

In this work, we merged several strategies in order to improve the photocurrent generation in hybrid solar cells using TiO_2 nanostructures and P3HT. First, we modified the surface of the TiO_2 nanoparticles with 2-TAA according to a procedure reported by our group.[13] In fact, the interface modified with TAA in the presence of the P3HT polymer was more efficient in promoting a better charge separation. Second, the sensitization of the titania film by the well-known ruthenium dyes (N3 or N719) is also an interesting approach to further improve the current generation in inverted TiO_2/P3HT solar cells.[22]

The synthetic route employed to prepare TiO_2 nanostructures, rods, and spheres was reported by Cozzoli et al.[5] During the synthesis, the Ti-O-Ti network is formed by several hydrolysis and polycondensation reactions. The differences between the two mechanisms (slow versus fast hydrolysis) allow the preparation of spherical or rod-like nanostructures, respectively. The XRD data in Figs. 1(a) and 1(b) exhibit diffraction peaks at 25.3 deg, 37.8 deg, and 48.0 deg that can be attributed, respectively, to the (101), (004), and (200) planes of the TiO_2 anatase structure. In the TiO_2 nanosphere sample, the diffraction peaks are wider because of the small size of these nanoparticles; while in the nanorod sample the peaks are better defined due to their higher aspect ratio. The lower ratio between the (101) and (004) planes in the TiO_2 NR sample in comparison to the TiO_2 NS sample is indicative of the formation of rod-like nanocrystals with a preferred growth orientation along the *c*-axis of the anatase lattice.[5]

Raman spectroscopy measurements [Figs. 1(c) and 1(d)] confirmed the vibrational modes of the anatase phase in both the TiO_2 NR and TiO_2 NS samples. Four of the six expected active modes[23] were identified in the nanorod sample, at 144 cm^{-1} (E_g), 399 cm^{-1} (B_{1g}), 513 cm^{-1} (A_{1g}), and 639 cm^{-1} (E_g). In the nanosphere sample, only the E_g and the A_{1g} modes could be observed. The absence of the other peaks is a consequence of the smaller size of the nanospheres.

The HRTEM images acquired for both the TiO_2 NR and TiO_2 NS samples show an aggregated morphology with no isolated particles (Fig. 2). This observation is in agreement with the ligand exchange procedure carried out to replace oleic acid by TAA molecules. However, it is possible to observe crystalline nanoparticles in both the TiO_2 NR and TiO_2 NS samples (nanospheres with ~4 nm, and nanorods with dimensions of ~3 and ~11 nm). SAXS experiments were performed to better define the size of the nanostructures, and the results are discussed in the next section.

Following ligand exchange with TAA, both the TiO_2 NR and TiO_2 NS samples were mixed with P3HT in the bulk heterojunction morphology. SAXS analysis of these films were performed before and after the incorporation of the inorganic nanostructures. The scattered intensity patterns shown in Fig. 3 were fitted using the Beaucage unified fit model,[19,20,21] which describes the scattering from a hierarchical structural level. This model considers only four parameters (G, R_g, B, and P) to define one structural level. The unified scattering function for each level can be defined as

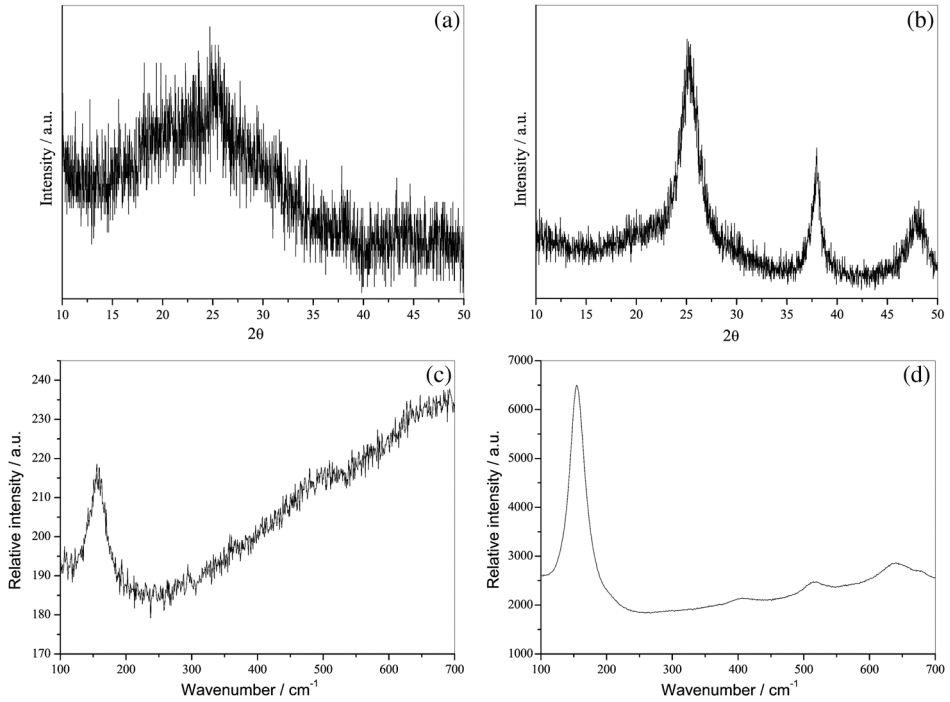

Fig. 1 X-ray diffraction (XRD) data and Raman spectra of TiO_2 NS (a) and (c) and TiO_2 NR (b) and (d) samples with thiopheneacetic acid (TAA) at surface.

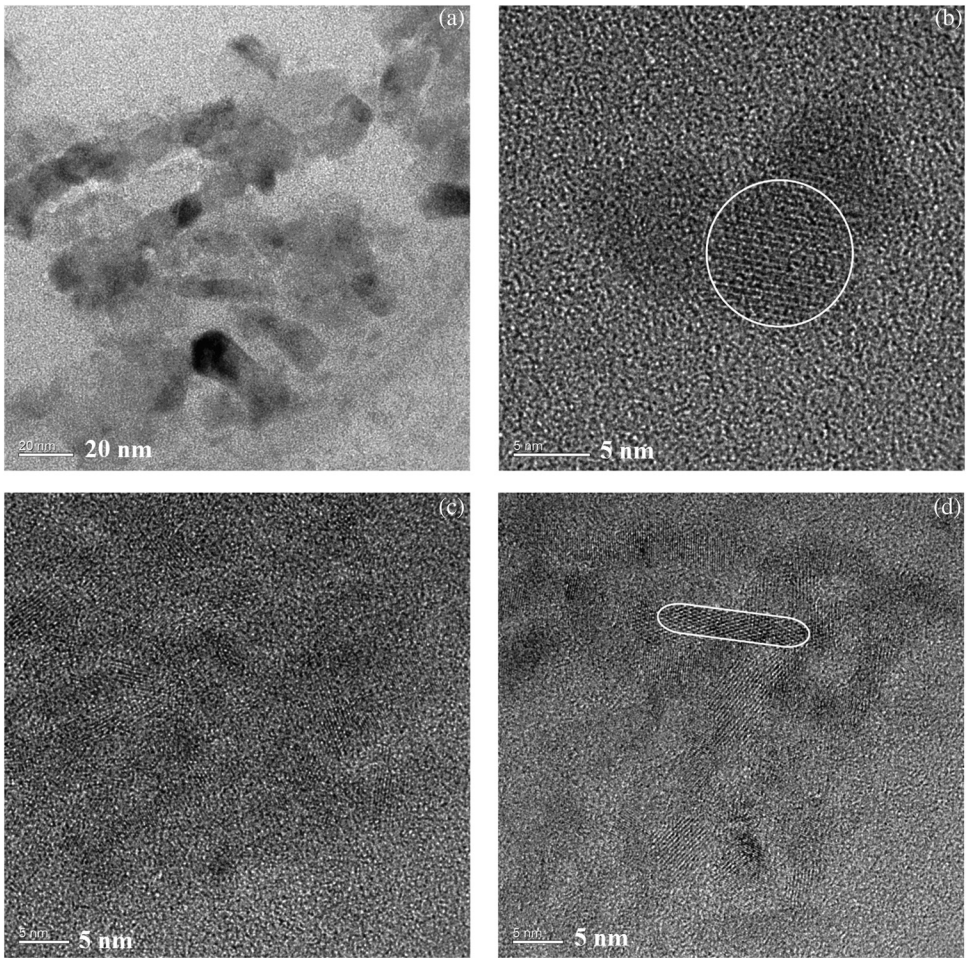

Fig. 2 High-resolution transmission electron microscopy (HRTEM) images of the TiO_2 NS/TAA (a) and (c) and TiO_2 NR/TAA samples (b) and (d) after dispersion by ultrasound in chloroform. The nanoparticles are capped by TAA molecules, a small ligand that allows particle aggregation.

$$I(q) = G\exp\left[\frac{(-q^2)(R_g{}^2)}{3}\right] + B\left\{\frac{q}{\left[\operatorname{erf}\left(\frac{qR_g}{\sqrt{6}}\right)\right]^3}\right\}^{-P},$$

where G is the Guinier prefactor, R_g is the radius of gyration, B is the Porod prefactor, and P is the power law.

Figure 3(a) presents the scattering pattern of the P3HT film, and the unified fit displays two structural levels. The first level gives a radius of gyration of 3.18 nm, which represents an average of the R_g of the P3HT polymeric chains. At high-q, a power law of approximately -2 corresponds to a mass fractal regime.

The scattering patterns of the inorganic nanostructure-containing films are shown in Figs. 3(b) and 3(c). Two distinct structural regimes are shown for the nanosphere-containing film [Fig. 3(b)]. The fitting gives a power law of -4 accounting for nanospheres with smooth surfaces. The size distribution of the nanospheres is shown in more detail in the inset. Nanosphere diameters vary between 2.0 and 4.5 nm, and the main population is centered at 3.3 nm. Comparing this result with the HRTEM images of the TiO_2 NS, it is possible to observe a better statistical representation of the population when the SAXS technique is used.

Three power law regimes are shown for the TiO_2 nanorod-containing film [Fig. 3(c)]. A power law of -1 is observed for the second level accounting for 1-D rods.[20] The size distribution obtained from the unified fitting (in the inset) shows two populations, one centered at 3.3 nm and the other centered at 9.8 nm, corresponding to the diameter and length of the nanorods,

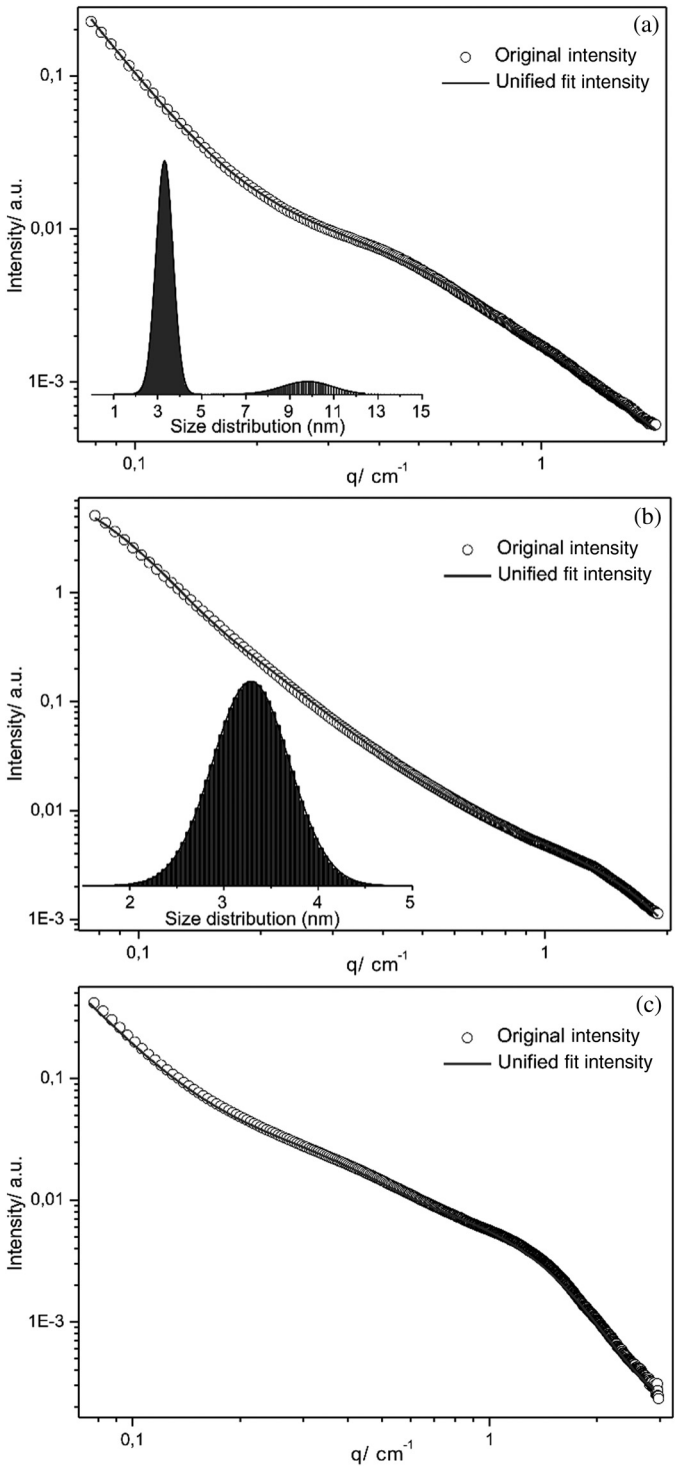

Fig. 3 Small-angle x-ray scattering (SAXS) profiles for the (a) poly(3-hexylthiophene) (P3HT), (b) P3HT/TiO_2 NS/TAA and (c) P3HT/TiO_2 NR/TAA films. The insets show the nanoparticle size distribution for both morphologies.

respectively. TiO_2 rods with a diameter and a length of this order are observed in the HRTEM images in Fig. 2(d).

The absorption profiles [Fig. 4(a)] of the nanocomposite films were similar when both TiO_2 morphologies were mixed to the P3HT polymer. For the pristine polymer, the maximum absorption is observed at 517 nm which corresponds to the $\pi - \pi^*$ absorption band of P3HT. This band

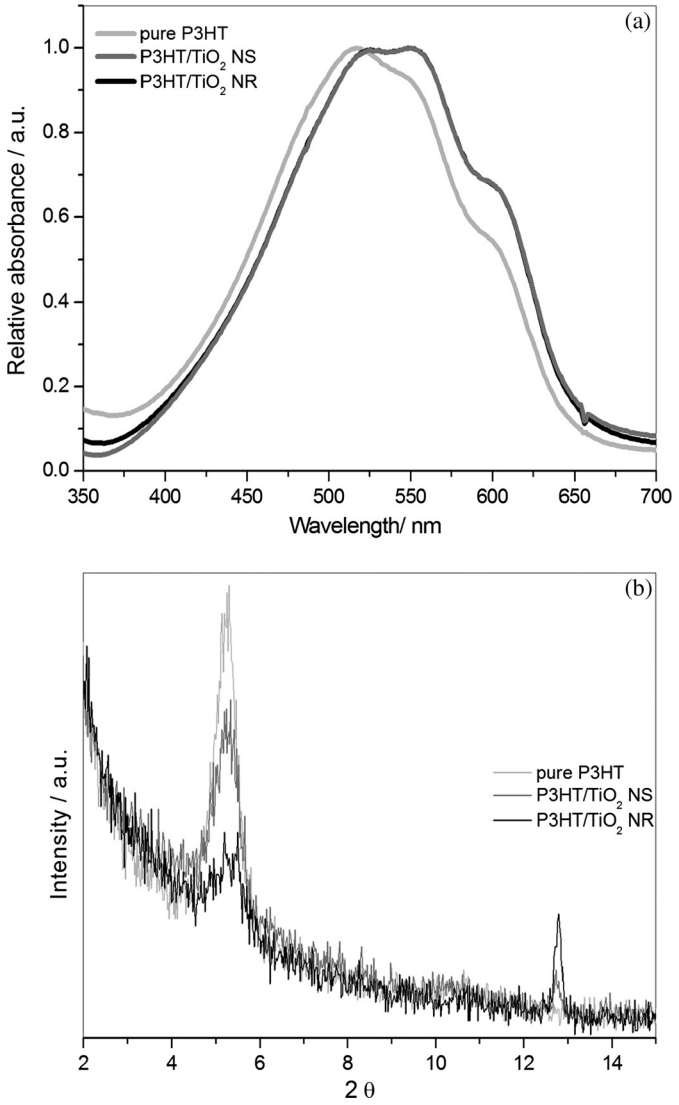

Fig. 4 (a) Absorption spectra and (b) XRD diffraction patterns of the P3HT, P3HT/TiO_2 NS/TAA, and P3HT/TiO_2 NR/TAA films deposited onto fluorine-doped tin oxide (FTO) substrates.

is red shifted to 526 nm in the presence of TiO_2 nanoparticles. In fact, the entire spectrum is shifted (including the two shoulders at ~550 and ~600 nm), thereby indicating that the insertion of nanostructures can promote a better polymer chain packing. In the other words, it is expected that the P3HT chains are flatter on (001) direction [inset on Fig. 4(b)], with a more effective conjugation.[24–26]

XRD analysis of the nanocomposites films showed differences in P3HT crystallinity [Fig. 4(b)]. The first-order reflection (100) at $2\theta = 5$ deg is observed with a high intensity in the P3HT film, and this peak can be related to the $\pi - \pi$ stacking.[25,27] The polymer presented a second-order reflection (200) at $2\theta = \sim 13$ deg, due to the interplanar distance between P3HT lamellas.[28] The half width of the (100) plane decreases after nanoparticle insertion, while the half width of the (200) increases. This is indicative of the decrease in the number of polymer crystals in the (100) direction. However, the (200) reflection refers to a short-range organization, indicating a strong interaction between polymer chains and nanoparticles that results in a good dispersion of the nanostrucutres in the polymer matrix.

The photoelectrochemical properties were measured by cyclic voltammetry, chronopotentiometry, and chronoamperometry techniques. Figure 5(a) shows higher current densities and higher capacity values for the films containing TiO_2 nanoparticles than the pristine P3HT film. This can be related to a better exciton dissociation and charge accumulation in the

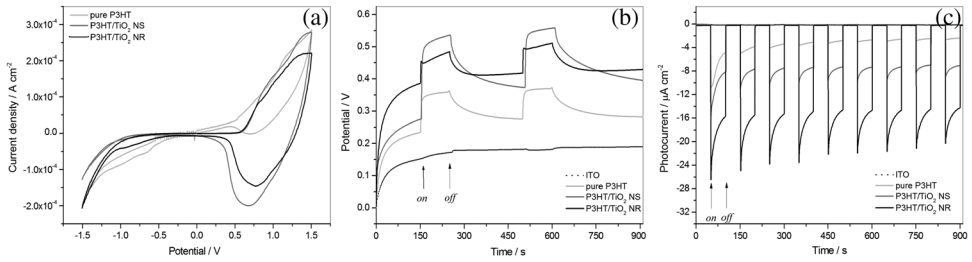

Fig. 5 Cyclic voltammetry (a), chronopotentiometry (b) and chronoamperometry experiments (c) of the P3HT, P3HT/TiO_2 NS, and P3HT/TiO_2 NR films. 1 mol L^{-1} solution of aqueous KCl containing 5×10^{-2} mol L^{-1} methylviologen was used as electrolyte. Light intensity of 100 mW cm^{-2}.

nanocomposite films. We calculated the highest occupied molecular orbital energy level of the samples (4.8 eV for the P3HT and 5.0 eV for P3HT/TiO_2 NS and P3HT/TiO_2 NR), which are consistent with the energy due to the electron transfer process from the polymer to the TiO_2 conduction band. The chronopotentiometry profiles presented in Fig. 5(b) show stable potentials for all samples under light on and off intervals. After illumination, the kinetics in V_{OC} response was fast, with reproducible values for the P3HT/TiO_2 NS and P3HT/TiO_2 NR films. Chronoamperometric profiles are exhibited in Fig. 5(c). The addition of the titania nanostructures in the P3HT film increases the photocurrent as expected because the inorganic nanoparticles act as electron acceptors, increasing both exciton dissociation and the charge-carrier transport. As observed in Fig. 5(c), all samples exhibit cathodic photocurrent, evidencing the *p*-type character of these films as observed in others systems.[29] This result indicates that the majority of charge carriers are holes that are driven to the platinum wire by the external circuit, while the minority of carriers (electrons) diffuses to the electrode/electrolyte interface.

The P3HT/TiO_2 NR film exhibited the highest photocurrent value (22 μA cm^{-2}), indicating a possible faster electronic transport due to the 1-D morphology of the nanorods. Their higher aspect ratio might also promote a better charge percolation to the electrodes.[1] However, not only the aspect ratio of the nanostructure must be taken into account but also the morphology of the nanocomposite films. Atomic force microscope images in the noncontact mode of P3HT, P3HT/TiO_2 NS, and P3HT/TiO_2 NR films were obtained (data not shown). Although the surface morphology is similar, the P3HT/TiO_2 NR film has lower roughness (rms) values (44.8 nm) in comparison to P3HT (60.9 nm) and P3HT/TiO_2 NS (69.0 nm) films. The smoother morphology after the incorporation of the titania nanorods is in agreement with the XRD data that show more planarity and extended conjugation of the P3HT polymer chains. It is difficult to quantitatively separate both contributions, and we believe that the two coexist and are important for the success of the photovoltaic device.

Figure 6 shows the I-V curves for the hybrid solar cells in the inverted configuration: FTO/TiO_2 compact/TiO_2 porous sensitized with the dye N719/P3HT layer mixed or not with TiO_2 NR/TAA and TiO_2 NS/TAA/PEDOT:PSS/Au. The figure also includes the schematic configuration of the device. Table 1 shows all the photovoltaic parameters.

The solar cells assembled with pristine P3HT and TiO_2 NS/TAA mixed with P3HT presented the same efficiency, with a difference in the photocurrent and FF values. In the device with only P3HT, FF is higher but the photocurrent is lower, in agreement with the photoelectrochemical experiments that show improved exciton dissociation after the incorporation of the inorganic nanostructures. FF values are lower in the solar cells with both TiO_2 NS/TAA and TiO_2 NR/TAA, indicating an increase in the series resistance of the active layer.

When devices using different TiO_2 morphologies are compared the solar cell assembled with TiO_2 NR/TAA displays higher efficiency, which is mainly attributed to the photocurrent values (also in accordance with the chronoamperometric experiments). The lower V_{OC} for this device, in comparison to that assembled with TiO_2 NS/TAA, can be an indication of faster recombination, in agreement with the chronopotentiometry experiment.

Several reports use P3HT and TiO_2 nanocrystals mixed in different film morphologies and in different device configurations. Taking as an example, for a hybrid solar cell in normal

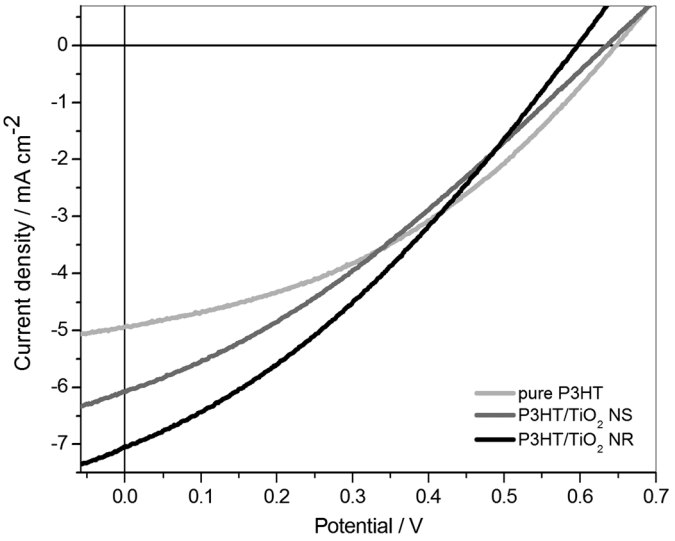

Fig. 6 Current versus voltage (I-V) curves for the hybrid solar cells in the configuration FTO/TiO_2 porous/N719 dye/P3HT (mixed or not with TiO_2 NS/TAA and TiO_2 NR/TAA/PEDOT:PSS/Au under 100 mW cm^{-2}. The inset shows the scheme of the inverted solar cell.

Table 1 Photovoltaic parameters of the solar cells.

	I_{SC}/mA cm^{-2}	V_{OC}/V	FF	η/%
P3HT	4.94 ± 0.2	0.65 ± 0.01	0.38 ± 0.01	1.22 ± 0.03
P3HT/TiO_2 NS/TAA	6.08 ± 0.3	0.64 ± 0.01	0.31 ± 0.01	1.21 ± 0.03
P3HT/TiO_2 NR/TAA	7.04 ± 0.4	0.60 ± 0.02	0.32 ± 0.01	1.35 ± 0.06

configuration, an efficiency of 2% was reported using absorbing molecules at TiO_2 nanorod surfaces.[15] When the inverted configuration was chosen and the active layer is composed exclusively of P3HT phase, the efficiency is lower than 1%.[12] However, the efficiency of the inverted hybrid solar cells can be improved by adding the TiO_2 nanocrystals as a third component in a bulk heterojunction with P3HT and PCBM.[7,30,31] In these solar cells, the TiO_2 nanocrystals represent an additional pathway for electron transport, and the efficiency can reach almost 4%.[30] The work by Liao et al.[32] is closest to ours. These authors introduced modified TiO_2 nanorods with pyridine or with an oligomer in a P3HT matrix. The solar cells assembled using the oligomer presented an efficiency of 1.2% ($I_{SC} = 3.8$ mA cm^{-2}, $V_{OC} = 0.62$ V and FF = 0.52). In our work, the sensitization of the TiO_2 mesoporous film by the N719 dye can explain the higher photocurrent values resulting in devices with a new efficiency record (1.35%).

4 Conclusions

In this work, two morphologies of TiO_2 nanostructures, nanorods and nanospheres, were synthetized and incorporated in inverted hybrid TiO_2/P3HT solar cells for the first time. Following ligand exchange, the nanoparticles aggregate as observed in the HRTEM images. On the other hand, when the nanoparticles are introduced in the P3HT matrix, SAXS experiments showed scattering centers in the same order of magnitude of the synthetized nanoparticles.

The P3HT/TiO_2 NR film exhibited the highest photocurrent values (22 μA cm^{-2}), indicating a possible faster electronic transport due to the 1-D morphology of the nanorods. In addition, the P3HT/TiO_2 NR film has lower roughness (rms) values (44.8 nm) in comparison to the P3HT (60.9 nm) and P3HT/TiO_2 NS (69.0 nm) films. The smoother morphology following the

incorporation of titania nanorods is in agreement with the XRD data that show more planarity and extended conjugation in the P3HT polymer chains. Comparing the devices using different TiO_2 morphologies, the solar cell assembled with TiO_2 NR/TAA displays higher efficiency, mainly attributed to the photocurrent values, reaching a record in the efficiency of 1.35%.

Acknowledgments

FSF and AFN thank the CNPq, FAPESP, and INEO agencies for financial support.

References

1. C.-K. Lee, C.-W. Pao, and C.-W. Chen, "Correlation of nanoscale organizations of polymer and nanocrystals in polymer/inorganic nanocrystal bulk heterojunction hybrid solar cells: insights from multiscale molecular simulations," *Energy Environ. Sci.* **6**, 307–315 (2013).
2. W. U. Huynh, J. J. Dittmer, and A. P. Alivisatos, "Hybrid nanorod: polymer solar cells," *Science* **295**, 2425–2427 (2002).
3. S. Sian and C.-W. Chen, "Polymer-metal-oxide hybrid solar cells," *J. Mater. Chem. A*, **1**, 10574–10591 (2013).
4. J. Das et al., "A facile nonaqueous route for fabricating titania nanorods and their viability in quasi-solid-state dye-sensitized solar cells," *J. Mater. Chem.* **20**, 4425–4431 (2010).
5. P. D. Cozzoli, A. Kornowski, and H. Weller, "Low-temperature synthesis of soluble and processable organic-capped anatase TiO_2 nanorods," *J. Am. Chem. Soc.* **125**, 14539–14548 (2003).
6. T. W. Zeng et al., "A large interconnecting network within hybrid MEH-PPV/TiO_2 nanorod photovoltaic devices," *Nanotechnology* **17**, 5387 (2006).
7. P. Yang et al., "TiO_2 nanowire electron transport pathways inside organic photovoltaics," *Phys. Chem. Chem. Phys.* **15**, 4566–4572 (2013).
8. Y. Lin et al., "Morphology control in TiO_2 nanorod/polythiophene composites for bulk heterojunction solar cells using hydrogen bonding," *Macromolecules* **45**, 8665–8673 (2012).
9. A. Ranjitha et al., "Inverted organic solar cells based on Cd-doped TiO_2 as an electron extraction layer," *Superlattices Microstruct.* **74**, 114–122 (2014).
10. M. Bolognesi et al., "The effect of selective contact electrodes on the interfacial charge recombination kinetics and device efficiency of organic polymer solar cells," *Phys. Chem. Chem. Phys.* **13**, 6105–6109 (2011).
11. G. K. Mor et al., "High efficiency double heterojunction polymer photovoltaic cells using highly ordered TiO_2 nanotube arrays," *Appl. Phys. Lett.* **91**, 152111 (2007).
12. M. Planells et al., "Oligothiophene interlayer effect on photocurrent generation for hybrid TiO_2/P3HT solar cells," *Appl. Mater. Interfaces* **6**, 17226–17235 (2014).
13. F. S. Freitas et al., "Tailoring the interface using thiophene small molecules in TiO_2/P3HT hybrid solar cells," *Phys. Chem. Chem. Phys.* **14**, 11990–11993 (2012).
14. K. Liu et al., "Efficient hybrid plasmonic polymer solar cells with Ag nanoparticle decorated TiO_2 nanorods embedded in the active layer," *Nanoscale* **6**, 6180–6186 (2014).
15. Y.-Y. Lin et al., "Interfacial nanostructuring on the performance of polymer/TiO_2 nanorod bulk heterojunction solar cells," *J. Am. Chem. Soc.* **131**, 3644–3649 (2009).
16. S. H. Eom et al., "Roles of interfacial modifiers in hybrid solar cells: inorganic/polymer bilayer versus inorganic/polymer: fullerene bulk heterojunction," *Appl. Mater. Interfaces* **6**, 803–810 (2014).
17. P. Ravirajan et al., "Hybrid polymer/zinc oxide photovoltaic devices with vertically oriented ZnO nanorods and an amphiphilic molecular interface layer," *J. Phys. Chem. B* **110**, 7635–7639 (2006).
18. A. Abate et al., "Protic ionic liquids as p-dopant for organic hole transporting materials and their application in high efficiency hybrid solar cells," *J. Am. Chem. Soc.* **135**, 13538–13548 (2013).
19. G. Beaucage, "Approximations leading to a unified exponential/power-law approach to small-angle scattering," *J. Appl. Cryst.* **28**, 717–728 (1995).

20. G. Beaucage, "Small-angle scattering from polymeric mass fractals of arbitrary mass-fractal dimension," *J. Appl. Cryst.* **29**, 134–146 (1996).
21. G. Beaucage, H. K. Kammler, and S. E. Pratsinis, "Particle size distributions from small-angle scattering using global scattering functions," *J. Appl. Cryst.* **37**, 523–535 (2004).
22. I. Khatri et al., "Similar device architectures for inverted organic solar cell and laminated solid-state dye-sensitized solar cells," *ISRN Electron.* **10** (2012) article ID 180787.
23. H. C. Choi, Y. M. Jung, and S. B. Kim, "Size effects in the Raman spectra of TiO_2 nanoparticles," *Vib. Spectrosc.* **37**, 33–38 (2005).
24. G. Li et al., "Polymer self-organization enhances photovoltaic efficiency," *J. Appl. Phys.* **98**, 43704 (2005).
25. T. Salim et al., "Solvent additives and their effects on blend morphologies of bulk heterojunctions," *J. Mater. Chem.* **21**, 242–250 (2011).
26. I. W. Hwang et al., "Carrier generation and transport in bulk heterojunction films processed with 1,8-octanedithiol as a processing additive," *J. Appl. Phys.* **104**, 033706 (2008).
27. H. Q. Nguyen et al., "Synthesis and characterization of a polyisoprene-b-polystyrene-b-poly (3-hexylthiophene) triblock copolymer," *Polym. Chem.* **4**, 462–465 (2013).
28. T. J. Prosa et al., "X-ray structural studies of poly(3-alkylthiophenes): an example of an inverse comb," *Macromolecules* **25**, 4364 (1992).
29. J. N. De Freitas et al., "Connecting the (quantum) dots: towards hybrid photovoltaic devices based on chalcogenide gels," *Phys. Chem. Chem. Phys.* **14**, 15180–15184 (2012).
30. P. Yang et al., "Identifying effects of TiO_2 nanowires inside bulk heterojunction organic photovoltaics on charge diffusion and recombination," *J. Mater. Chem. C* **2**, 4922–4927 (2014).
31. G. Grancini et al., "Boosting infrared light harvesting by molecular functionalization of metal oxide/polymer interfaces in efficient hybrid solar cells," *Adv. Funct. Mater.* **22**, 2160–2166 (2012).
32. H.-C. Liao et al., "Diketopyrrolopyrrole-based oligomer modified TiO_2 nanorods for air-stable and all solution processed poly(3-hexylthiophene): TiO_2 bulk heterojunction inverted solar cell," *J. Mater. Chem.* **22**, 10589–10596 (2012).

Flavio Santos Freitas received his PhD degree in chemistry from State University of Campinas (UNICAMP), Brazil, in 2013. Since 2013, he has been a professor at the Federal Institute of South of Minas Gerais (IFSULDEMINAS) and an associate researcher at the Laboratory of Nanotechnology and Solar Energy (LNES, UNICAMP). His research focuses on inorganic semiconductor applications with emphasis on hybrid solar cells.

Juliana Martins de Souza e Silva received her PhD degree in chemistry from Università degli Studi del Piemonte Orientale, Italy, in 2009. From 2009 to 2012, she was a postdoctoral fellow at State University of Campinas, Brazil, working with nanocatalysts. In 2012, she joined the Mateus Cardoso Group at the Brazilian Synchrotron Laboratory, where she worked on developing nanomaterials for biomedical applications. She recently joined the chair of biomedical physics at Technische Universität München, Germany.

Mateus Borba Cardoso received his PhD degrees in physical chemistry from Federal University of Rio Grande do Sul, Brazil, and polymer chemistry from Joseph Fourier University, France, in 2007. In 2008 and 2009, he was a postdoctoral fellow at Oak Ridge National Laboratory, USA. Since 2009 he has been an associate researcher at the Brazilian Synchrotron Laboratory, Brazil. His present research interests include the development of smart composite materials and their characterization through x-ray techniques.

Ana Flavia Nogueira received her PhD degree in chemistry from the State University of Campinas (UNICAMP), Campinas, Brazil, in 2001. In 2002, she joined the group of Professor James R. Durrant at Imperial College, London, in a postdoctoral position. Since 2004, she has been an associate professor at UNICAMP. She is also the coordinator of the Laboratory of Nanotechnology and Solar Energy (LNES), a leading group in third-generation solar cells in Brazil.